Frontiers of Information Technology & Electronic Engineering
www.jzus.zju.edu.cn; engineering.cae.cn; www.springerlink.com
ISSN 2095-9184 (print); ISSN 2095-9230 (online)
E-mail: jzus@zju.edu.cn

Near-field joint estimation of multi-targets' position and velocity in a terahertz MIMO-OFDM system based on tensor decomposition*

Ke LIU[1], Shengfu ZHAO[1], Weixin CHEN[1], Zhen WANG[1,2], Lingxiang LI[†‡1], Zhi CHEN[1], Qiang XU[1]

[1]*National Key Laboratory of Wireless Communications, University of Electronic Science and Technology of China, Chengdu 611731, China*

[2]*School of Electrical Engineering and Information, Southwest Petroleum University, Chengdu 610500, China*

[†]E-mail: lingxiang.li@uestc.edu.cn

Received June 2, 2024; Revision accepted Sept. 30, 2024; Crosschecked Nov. 25, 2024

Abstract: This paper investigates the joint estimation of multi-targets' position and velocity for a terahertz multi-input multi-output (MIMO) orthogonal frequency division multiplexing (OFDM) system operating in the near field based on tensor decomposition. The waveforms transmitted from shared antennas carry communication messages and are orthogonal to each other in the frequency domain. The estimation of the position and velocity of multiple targets in the considered near-field scenario is challenging because it involves spherical wavefronts. A signal model based on spherical wavefronts enables higher resolution on spatial position, which, if properly designed, can be used to improve the estimation accuracy. In this paper, we propose a CANDECOMP/PARAFAC (CP) decomposition-based near-field localization (CP-NFL) algorithm for the joint estimation of the position and velocity of multiple targets. In our proposed method, the received signal is expressed as a third-order tensor; based on its factor matrices we convert the original non-convex optimization problem into a convex one and solve it with CVX tools. Our analysis reveals that the uniqueness in CP decomposition can be guaranteed and the computational complexity of our proposed method is linear to the sum of the third powers of the number of sub-carriers, OFDM symbols, antennas, and targets. Numerical results show that our proposed method has a clear advantage over the existing method in terms of estimation accuracy and computational complexity.

Key words: Terahertz; Multi-input multi-output orthogonal frequency division multiplexing (MIMO-OFDM); Near-field localization (NFL); Velocity estimation; Tensor decomposition

https://doi.org/10.1631/FITEE.2400472 **CLC number:** TN95

1 Introduction

The demand for ubiquitous, reliable, fast, and scalable wireless services is pushing today's radio technology toward its ultimate limits (Akyildiz et al., 2020). In this context, it is natural to continue searching for more bandwidth, which in turn pushes the operation toward higher frequencies. Terahertz communications in the band from 0.1 THz to 10 THz is considered as a highly promising technology for 6G (the sixth generation of wireless communications) and beyond (Akyildiz et al., 2022). Meanwhile, communications and radar systems that used to operate independently are now evolving toward integrated sensing and communications (ISAC) systems (Zhang JA et al., 2021). Due to the availability of hundreds of gigahertz-spectrum resources, terahertz communications can provide significant communication capacity and high-precision perception, making terahertz ISAC an attractive research topic (Sarieddeen et al., 2021; Chen H et al., 2022).

‡ Corresponding author

* Project supported by the National Natural Science Foundation of China (Nos. 62271121 and 62301465)

ORCID: Lingxiang LI, https://orcid.org/0000-0002-8600-4461

The use of high frequencies translates into higher path losses per antenna, which can be compensated for by antenna arrays (Xiao et al., 2017). This combination undermines the fundamental far-field assumption of multiple antenna communications; i.e., the wavefronts of radiated waves are locally planar over antenna arrays (Zhao et al., 2023; Alhafid et al., 2024). Instead, when the detection range is less than the Rayleigh distance of $\frac{2D_{\mathrm{R}}^2}{\lambda}$, where D_{R} is the antenna aperture and λ denotes the wavelength, the near-field region should be considered and wavefronts of radiated waves are spherical over antenna arrays (Cui et al., 2023; Zhang HY et al., 2022, 2023; Gao et al., 2024). This essential feature causes terahertz arrays to possess both azimuth and distance resolutions. Many existing algorithms make use of spherical wavefronts to enhance positioning accuracy (Singh et al., 2016, 2017; Podkurkov et al., 2018; Zhang XF et al., 2018; Zuo et al., 2019; Pan et al., 2021; Rinchi et al., 2022). Along this line of research, existing works make a trade-off between complexity and parameter estimation accuracy. Specifically, several authors (Zhang XF et al., 2018; Zuo et al., 2019; Pan et al., 2021; Rinchi et al., 2022) approximated the signal model in the near-field array using a second-order Taylor expansion to avoid the computational complexity of parameter estimation, while other authors (Singh et al., 2016, 2017; Podkurkov et al., 2018) used precise near-field spherical wave information for positioning, avoiding the loss of detection accuracy caused by model approximation.

However, the aforementioned positioning methods are based on radar chirp waveforms, whereas orthogonal frequency division multiplexing (OFDM) waveforms are more commonly used in communications. Most importantly, in the foreseeable future, mobile communication protocols will continue to rely on OFDM waveforms. In this study, we consider using OFDM waveforms. Due to the differences in signal generation and formats, the principles of parameter estimation based on OFDM waveforms differ from those based on radar chirp waveforms. Specifically, the traditional radar systems first mix the received signal with a reference signal before the analog-to-digital converter (ADC), based on which they derive the target's position, azimuth, and velocity by analyzing the relationship between the resulting signal frequency and propagation time delay (Tsujimura and Mori, 2022). In contrast, systems based on OFDM waveforms cannot directly decorrelate the signal before the ADC because the instantaneous signal is a multicarrier signal. Instead, the entire broadband signal must be sampled using an ADC, and the target's position, azimuth, and velocity information are further extracted (Gaudio et al., 2019).

In far-field array scenarios, parameter estimation based on OFDM waveforms is well-established. Works by Liu et al. (2017), Knill et al. (2019), Sanson et al. (2019), Temiz et al. (2021), Tian et al. (2021), and Wan et al. (2023) have used the phase differences between sub-carriers, antennas, and symbols for position, azimuth, and velocity estimation. However, in near-field array scenarios, the phase difference between antennas is related not only to azimuth but also to the distance between the array and the target, increasing the complexity of parameter estimation (Podkurkov et al., 2021; Sakhnini et al., 2022). Specifically, Podkurkov et al. (2021) used a method of passive sensing at the base station, processed OFDM uplink signals at the base station, and used precise near-field spherical wavefront information to achieve target positioning. Sakhnini et al. (2022) adopted an active sensing method, using time-division OFDM where each antenna transmits OFDM symbols in a time-multiplexed manner. This scheme requires the antenna spacing in the uniform linear array (ULA) to be within one wavelength to avoid position ambiguity and uses maximum likelihood estimation, resulting in high algorithmic complexity.

Different from the aforementioned works, this study uses frequency-orthogonal OFDM (FO-OFDM) signals, where the waveform transmitted from each antenna is orthogonal in the frequency domain for near-field target positioning and velocity estimation. The specific contributions are as follows:

1. By transmitting FO-OFDM signals from the transmitting antennas and combining them at the receiving end, wideband positioning is achieved and positioning accuracy improves. Additionally, by shifting the ambiguity constraint from the conventional within-one-wavelength antenna spacing (Sakhnini et al., 2022) to the used signal bandwidth, the antenna scanning range is increased.

2. Based on the established near-field signal model, we reconstruct the received data in a third-order tensor

form. We then propose a CANDE-COMP/PARAFAC (CP) decomposition-based near-field localization (CP-NFL) algorithm, where multi-dimensional information such as phase differences between antennas and sub-carriers is jointly processed to enhance the accuracy of target localization estimation.

3. To reduce the complexity of the tensor decomposition algorithm, we separate the transmit and receive arrays into different groups. Analyses show that the computational complexity of the proposed method is linear to the sum of the third powers of the number of sub-carriers, OFDM symbols, antennas, and targets. Numerical results show the effectiveness of the proposed method.

Notations: $\boldsymbol{a}$ represents a vector, $\boldsymbol{A}$ represents a matrix, $\boldsymbol{\mathcal{A}}$ represents a tensor. $a(i)$ denotes the i^{th} element of vector $\boldsymbol{a}$. Also, we use $\boldsymbol{B}=\boldsymbol{a}\circ\boldsymbol{b}$ to denote the outer product between the vectors $\boldsymbol{a}\in\mathbb{C}^I$ and $\boldsymbol{b}\in\mathbb{C}^J$, which results in matrix $\boldsymbol{B}$ of size $I\times J$ with $B_{ij}=a(i)b(j)$. Moreover, $\angle\boldsymbol{a}$ denotes the vector of principal angles of complex vector $\boldsymbol{a}$. $\|\boldsymbol{A}\|_{\text{F}}$ defines the Frobenius norm of matrix $\boldsymbol{A}$.

2 System model and problem formulation

Consider a multi-input multi-output (MIMO) OFDM ISAC system with a ULA surveilling the area shown in Fig. 1. The ULA is divided into two groups, where the left group is for the transmitter and the right group is for the receiver, with M_{T} and Q_{R} antenna elements, respectively. The antenna element spacing is assumed to be d, so the sizes of the transmit and receive arrays are $D_{\text{T}}=(M_{\text{T}}-1)d$ and $D_{\text{R}}=(Q_{\text{R}}-1)d$, respectively.

As mentioned previously, for terahertz ISAC systems, the antenna array usually works in the near-field array region, where the spherical wavefront should be considered and the analytical signal model becomes very complex. A far-field and near-field hybrid is considered, where we divide the transmit and receive antenna arrays into U_{T} and U_{R} sub-arrays, each of which is equipped with M and Q antenna elements, respectively. Therefore, it holds true that $M_{\text{T}}=U_{\text{T}}M$ and $Q_{\text{R}}=U_{\text{R}}Q$.

The location of the transmit and receive antenna is defined in two-dimensional Cartesian coordinates with respect to the origin. Assume that the transmit and receive array are both located on the X-axis. The coordinates of the $m_{u_{\text{t}}}^{\text{th}}$ antenna element in the u_{t}^{th} transmit sub-array and that for the $q_{u_{\text{r}}}^{\text{th}}$ antenna element in the u_{r}^{th} receive sub-array are given as

$$(x_{\text{T},m_{u_{\text{t}}}},0),u_{\text{t}}=1,2,\cdots,U_{\text{T}},m_{u_{\text{t}}}\in\big((u_{\text{t}}-1)M,u_{\text{t}}M-1\big), \tag{1}$$

$$(x_{\text{R},q_{u_{\text{r}}}},0),u_{\text{r}}=1,2,\cdots,U_{\text{R}},q_{u_{\text{r}}}\in\big((u_{\text{r}}-1)Q,u_{\text{r}}Q-1\big). \tag{2}$$

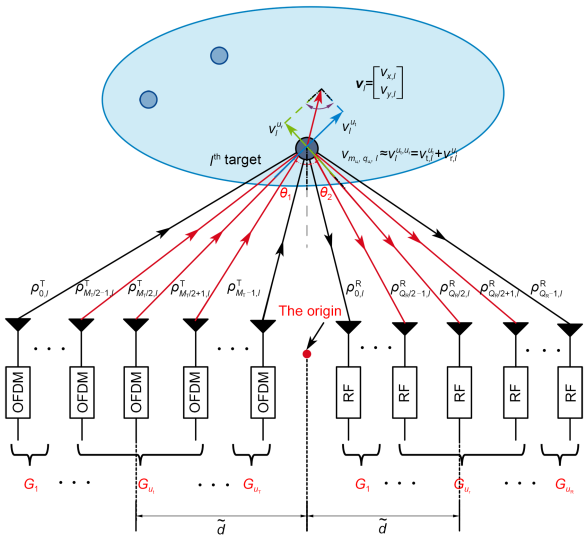

Fig. 1 Illustration of the near-field uniform linear array (ULA) model

Specifically, the coordinates of the center antenna element of the transmit and receive array are $(x_{M_T/2}, 0)$ and $(x_{Q_R/2}, 0)$. Let the l^{th} (l=1, 2, ⋯, L) target locate at (x_l, y_l), whose moving velocity is ($v_{x,l}$, $v_{y,l}$). In this study, we aim to estimate the parameters, (x_l, y_l) and ($v_{x,l}$, $v_{y,l}$), $\forall\, l$, based on the observed signals reflected from the target.

To accomplish this, the transmitter sends FO-OFDM signals. The FO-OFDM signal contributed from the $m_{u_t}^{\text{th}}$ transmit antenna element contains P symbols and each symbol is composed of N sub-carriers with uniform spacing of Δf. Each OFDM symbol duration is $T_0=T+T_{\text{cp}}$, where T and T_{cp} denote the duration of the data and guard interval, respectively, to avoid inter-symbol interference (ISI) (Zhang RY et al., 2023). Thus, the waveform transmitted by the $m_{u_t}^{\text{th}}$ transmit antenna at time t is (Gaudio et al., 2019)

$$s_{m_{u_t}}(t)=\mathrm{e}^{\mathrm{j}2\pi f_c t}\sum_{p=0}^{P-1}\sum_{n=0}^{N-1}\tilde{s}_{m_{u_t},n,p}\mathrm{e}^{\mathrm{j}2\pi\left(n+m_{u_t}K\right)\Delta f\left(t-pT_0-T_{\text{cp}}\right)}\cdot\mathrm{rect}\left[\frac{t-pT_0}{T_0}\right],\tag{3}$$

where f_c denotes carrier frequency, p is the OFDM symbol index, and n is the sub-carrier index. The symbol $\tilde{s}_{m_{u_t},n,p}$ is modulated on the n^{th} sub-carrier of the p^{th} OFDM symbol for the $m_{u_t}^{\text{th}}$ transmitting antenna. K is an integer whose value should be greater than N such that the waveform from each antenna does not intersect in the frequency domain. The rectangle function rect[t] equals 1 for $t\in[0, T_0]$ and 0 otherwise.

The transmitted signal reaches the receiving end after being reflected by targets. Because the signals transmitted from different antennas are orthogonal in the frequency domain, we consider bandpass filters at the receiver to separate signals from different transmitting antennas. In addition, for the considered terahertz system, the carrier frequency is hundreds of gigahertz, while the signal bandwidth is approximately several gigahertz. The latter is much smaller than the former; consequently in the signal model we only consider the impact of the Doppler frequency shift caused by the carrier frequency and assume a constant Doppler shift over the entire signal bandwidth. The reflected signal from the $m_{u_t}^{\text{th}}$ transmitting antenna to the $q_{u_r}^{\text{th}}$ receiving antenna can thus be expressed as

$$y_{m_{u_t},q_{u_r}}(t)=\sum_{l=1}^{L}\alpha_l\mathrm{e}^{\mathrm{j}2\pi\left(f_c+f_l^{\text{D}}\right)\left(t-\tau_{m_{u_t},q_{u_r},l}\right)}s_{m_{u_t}}\left(t-\tau_{m_{u_t},q_{u_r},l}\right)+z_{m_{u_t},q_{u_r}}(t),\tag{4}$$

where α_l represents the path loss from the transmitter to the receiver related to the l^{th} target, which remains almost constant during the observation time. $f_l^{\text{D}}=\dfrac{2v_{m_{u_t},q_{u_r},l}f_c}{c}$ is defined as the Doppler shift, where c denotes the speed of light and $v_{m_{u_t},q_{u_r},l}$ is the velocity along the wavefront propagation path from the $m_{u_t}^{\text{th}}$ transmit antenna to the $q_{u_r}^{\text{th}}$ receive antenna related to the l^{th} target. We estimate and observe the velocity based on Doppler shift. For a target moving in the near-field array scenario, the Doppler shift from different signal propagation paths is different, and the observed velocity is different. In addition, $\tau_{m_{u_t},q_{u_r},l}$ represents the propagation time delay and $z_{m_{u_t},q_{u_r}}(t)$ denotes the additive white Gaussian noise (AWGN).

Let $R_{m_{u_t},q_{u_r},l}$ be the propagation path length from the $m_{u_t}^{\text{th}}$ transmitting antenna to the l^{th} target. After being reflected to the $q_{u_r}^{\text{th}}$ receiving antenna, the propagation time delay can be expressed as

$$\tau_{m_{u_t},q_{u_r},l}=R_{m_{u_t},q_{u_r},l}/c=\left(\sqrt{\left(x_l-x_{\text{T},m_{u_t}}\right)^2+y_l^2}+\sqrt{\left(x_l-x_{\text{R},q_{u_r}}\right)^2+y_l^2}\right)\Big/c.\tag{5}$$

For the convenience of analysis in the following context, let $\delta_{m_{u_t},l}^{\text{T}}$ be the path difference between the $m_{u_t}^{\text{th}}$ antenna to the target and the $(M_T/2)^{\text{th}}$ transmit antenna to the target, and $\delta_{q_{u_r},l}^{\text{R}}$ be the path differences between the $q_{u_r}^{\text{th}}$ antenna to the target and the $(Q_R/2)^{\text{th}}$ receive antenna to the target, i.e.,

$$\delta_{m_{u_t},l}^{\text{T}}=\sqrt{\left(x_l-x_{\text{T},m_{u_t}}\right)^2+y_l^2}-\rho_{M_T/2,l}^{\text{T}},\tag{6}$$

$$\delta_{q_{u_r},l}^{\text{R}}=\sqrt{\left(x_l-x_{\text{R},q_{u_r}}\right)^2+y_l^2}-\rho_{Q_R/2,l}^{\text{R}},\tag{7}$$

where

$$\rho_{M_T/2,l}^{\text{T}}=\sqrt{\left(x_l-x_{\text{T},M_T/2}\right)^2+y_l^2},\tag{8}$$

$$\rho_{Q_R/2,l}^{\text{R}}=\sqrt{\left(x_l-x_{\text{R},Q_R/2}\right)^2+y_l^2}.\tag{9}$$

On the other hand, let

$$\tau_{M_{\mathrm{T}}/2,\,Q_{\mathrm{R}}/2,\,l}=\left(\rho^{\mathrm{T}}_{M_{\mathrm{T}}/2,\,l}+\rho^{\mathrm{R}}_{Q_{\mathrm{R}}/2,\,l}\right)\Big/c. \tag{10}$$

Then Eq. (5) can be rewritten as

$$\tau_{m_{u_t},q_{u_t},l}=\tau_{M_{\mathrm{T}}/2,\,Q_{\mathrm{R}}/2,\,l}+\left(\delta^{\mathrm{T}}_{m_{u_t},l}+\delta^{\mathrm{R}}_{q_{u_t},l}\right)\Big/c. \tag{11}$$

Furthermore, by sampling the waveform in Eq. (4) and removing the guard interval at the receiver, the resulting signal at time iT/N of the p^{th} OFDM symbol is

$$\begin{aligned}y_{m_{u_t},q_{u_t},p}(i)&=y_{m_{u_t},q_{u_t}}(t)\big|_{t=pT_0+T_{\mathrm{cp}}+iT/N}\\&=\sum_{l=1}^{L}\sum_{n=0}^{N-1}\alpha_l\,\tilde{s}_{m_{u_t},n,p}\,\mathrm{e}^{-\mathrm{j}2\pi f_{\mathrm{c}}\left(\tau_{M_{\mathrm{T}}/2,\,Q_{\mathrm{R}}/2,\,l}+\frac{\delta^{\mathrm{R}}_{q_{u_t},l}+\delta^{\mathrm{T}}_{m_{u_t},l}}{c}\right)}\\&\quad\cdot\mathrm{e}^{\mathrm{j}2\pi\left(\frac{2v_{m_{u_t},q_{u_t},l}f_{\mathrm{c}}}{c}\right)\left(pT_0+iT/N-\tau_{m_{u_t},q_{u_t},l}\right)}\\&\quad\cdot\mathrm{e}^{\mathrm{j}2\pi\left(n+Km_{u_t}\right)\Delta f\left(iT/N-\tau_{M_{\mathrm{T}}/2,\,Q_{\mathrm{R}}/2,\,l}-\frac{\delta^{\mathrm{R}}_{q_{u_t},l}+\delta^{\mathrm{T}}_{m_{u_t},l}}{c}\right)}\\&\quad+z_{m_{u_t},q_{u_t},p}(i),\ i=0,1,\cdots,N-1.\end{aligned} \tag{12}$$

To simplify the analysis, we make assumptions as follows:

Assumption 1 The antenna aperture $D_{\mathrm{T}}+D_{\mathrm{R}}$ is small enough compared with $\frac{c}{N\Delta f}$ (Cohen et al., 2018). As $\delta^{\mathrm{R}}_{q_{u_t},l}+\delta^{\mathrm{T}}_{m_{u_t},l}\le D_{\mathrm{T}}+D_{\mathrm{R}}$, it holds true that

$$N\Delta f\,\frac{\delta^{\mathrm{R}}_{q_{u_t},l}+\delta^{\mathrm{T}}_{m_{u_t},l}}{c}\ll 1. \tag{13}$$

Therefore, the effect of $\mathrm{e}^{\mathrm{j}2\pi n\Delta f\frac{\delta^{\mathrm{R}}_{q_{u_t},l}+\delta^{\mathrm{T}}_{m_{u_t},l}}{c}}$ in Eq. (12) can be ignored.

Assumption 2 The propagation time delay is small enough compared with the symbol duration T_0 (Gaudio et al., 2019), i.e.,

$$\tau_{m_{u_t},q_{u_t},l}\ll T_0. \tag{14}$$

Therefore, the term $\mathrm{e}^{-\mathrm{j}2\pi\frac{2v_{m_{u_t},q_{u_t},l}f_{\mathrm{c}}\tau_{m_{u_t},q_{u_t},l}}{c}}$ in Eq. (12) can be ignored.

Assumption 3 The speed of the targets relative to the same sub-array antenna is roughly equal, i.e.,

$$v_{m_{u_t},q_{u_t},l}\approx v^{u_t,u_t}_{l}. \tag{15}$$

These simplify our signal model and subsequent parameter estimation process.

As a result of Assumptions 1–3, the expression in Eq. (12) can be approximated as

$$\begin{aligned}y_{m_{u_t},q_{u_t},p}(i)=&\sum_{l=1}^{L}\sum_{n=0}^{N-1}\alpha_l\tilde{s}_{m_{u_t},n,p}\,\mathrm{e}^{-\mathrm{j}2\pi f_{\mathrm{c}}\left(\tau_{M_{\mathrm{T}}/2,\,Q_{\mathrm{R}}/2,\,l}+\frac{\delta^{\mathrm{R}}_{q_{u_t},l}+\delta^{\mathrm{T}}_{m_{u_t},l}}{c}\right)}\\&\cdot\mathrm{e}^{\mathrm{j}2\pi\left(\frac{2v^{u_t,u_t}_{l}f_{\mathrm{c}}}{c}\right)\left(pT_0+iT/N\right)}\\&\cdot\mathrm{e}^{\mathrm{j}2\pi\left(n+Km_{u_t}\right)\Delta f\left(iT/N-\tau_{M_{\mathrm{T}}/2,\,Q_{\mathrm{R}}/2,\,l}\right)}\\&\cdot\mathrm{e}^{-\mathrm{j}2\pi Km_{u_t}\left(\frac{\delta^{\mathrm{R}}_{q_{u_t},l}+\delta^{\mathrm{T}}_{m_{u_t},l}}{c}\right)}\\&+z_{m_{u_t},q_{u_t},p}(i),\ i=0,1,\cdots,N-1.\end{aligned} \tag{16}$$

Performing a discrete Fourier transform (DFT) on $y_{m_{u_t},q_{u_t},p}(i)$, $i=0,1,\cdots,N-1$, we arrive at (Gaudio et al., 2019)

$$\begin{aligned}y_{m_{u_t},q_{u_t},p,n}&=\frac{1}{N}\sum_{i=0}^{N-1}y_{m_{u_t},q_{u_t},p}(i)\,\mathrm{e}^{-\mathrm{j}2\pi\frac{ni}{N}}\\&\approx\sum_{l=1}^{L}\beta_l\,\mathrm{e}^{-\mathrm{j}2\pi n\Delta f\tau_{M_{\mathrm{T}}/2,\,Q_{\mathrm{R}}/2,\,l}}\mathrm{e}^{\mathrm{j}2\pi f_{\mathrm{c}}\left(\frac{2v^{u_t,u_t}_{l}pT_0}{c}\right)}\\&\quad\cdot\gamma_{m_{u_t},q_{u_t},l}+z_{m_{u_t},q_{u_t},p,n},\end{aligned} \tag{17}$$

in which

$$\beta_l=\alpha_l\mathrm{e}^{-\mathrm{j}2\pi f_{\mathrm{c}}\tau_{M_{\mathrm{T}}/2,\,Q_{\mathrm{R}}/2,\,l}}\tilde{s}_{m_{u_t},n,p}, \tag{18}$$

$$\gamma_{m_{u_t},q_{u_t},l}=\mathrm{e}^{-\mathrm{j}2\pi Km_{u_t}\Delta f\left(\tau_{M_{\mathrm{T}}/2,\,Q_{\mathrm{R}}/2,\,l}+\frac{\delta^{\mathrm{T}}_{m_{u_t},l}}{c}+\frac{\delta^{\mathrm{R}}_{q_{u_t},l}}{c}\right)}\mathrm{e}^{-\mathrm{j}2\pi f_{\mathrm{c}}\left(\frac{\delta^{\mathrm{T}}_{m_{u_t},l}}{c}+\frac{\delta^{\mathrm{R}}_{q_{u_t},l}}{c}\right)}. \tag{19}$$

From Eq. (19), one can see that if the phase of $2\pi\frac{K\Delta f}{c}\delta^{\mathrm{R}}_{q_{u_t},l}$ exceeds $[-\pi,\pi]$, it will cause phase ambiguity, resulting in inaccurate estimation of $\delta^{\mathrm{R}}_{q_{u_t},l}$. Otherwise, when the condition $-\pi\le 2\pi\frac{K\Delta f}{c}\delta^{\mathrm{R}}_{q_{u_t},l}\le\pi$ is met, $\delta^{\mathrm{R}}_{q_{u_t},l}$ can be solved without ambiguity. On the other hand, it holds true that $\delta^{\mathrm{R}}_{q_{u_t},l}\le\frac{Q_{\mathrm{R}}d}{2}$. The combination of the above two equations indicates that if $d\le\frac{c}{2Q_{\mathrm{R}}\Delta fK}$, there is no ambiguity concerning the estimation of $\delta^{\mathrm{R}}_{q_{u_t},l}$. In general, we have $\frac{c}{Q_{\mathrm{R}}\Delta fK}\gg\frac{c}{f_{\mathrm{c}}}=\lambda$; thus, shifting the ambiguity constraints from the conventional within-one-wavelength antenna spacing to the used signal bandwidth and increasing the scanning range of the antennas resolve the position ambiguity issue.

Our objective is to estimate $\{(x_l, y_l)\}$ and $\{(v_{x,l}, v_{y,l})\}$ from the noise-corrupted observations $\{y_{m_{u_t},q_{u_r},p,n}\}$. Due to the coupled characteristics of $\{(x_l, y_l)\}$ and $\{(v_{x,l}, v_{y,l})\}$ in the observed data, it is difficult to directly extract them from Eq. (17). In the following context, we will first organize the observed samples $y_{m_{u_t},q_{u_r},p,n}$ as an incomplete structured third-order tensor. Then, the unknown parameters $\{(x_l, y_l)\}$ and $\{(v_{x,l}, v_{y,l})\}$ can be estimated by analyzing the factor matrices obtained from the CP decomposition of this incomplete tensor.

3 Joint estimation of position and velocity based on CP decomposition

In this section, we propose the CP-NFL algorithm based on tensor decomposition to achieve high-accuracy parameter estimation. This algorithm mainly consists of three steps: tensor formulation, tensor decomposition, and parameter estimation. Each step is described, and the computational complexity of the proposed CP-NFL algorithm is analyzed.

3.1 Tensor formulation and CP decomposition

Because the transmitter and the radar receiver in the considered system are co-located, it is reasonable to assume that the transmitted messages $\tilde{s}_{m_{u_t},n,p}$ are known at the radar receiver. We remove $\tilde{s}_{m_{u_t},n,p}$ from the observed data $y_{m_{u_t},q_{u_r},p,n}$ and arrive at $\tilde{y}_{m_{u_t},q_{u_r},p,n}=y_{m_{u_t},q_{u_r},p,n}/\tilde{s}_{m_{u_t},n,p}$. This, combined with the Eq. (17), indicates that

$$\begin{aligned}\tilde{y}_{m_{u_t},q_{u_r},p,n}=&\sum_{l=1}^{L}\tilde{\beta}_l \mathrm{e}^{-\mathrm{j}2\pi n\Delta f\tau_{M_T/2,Q_R/2,l}}\\&\cdot\mathrm{e}^{\mathrm{j}2\pi f_c\left(\frac{2v_l^{u_t,u_t}pT_0}{c}\right)}\gamma_{m_{u_t},q_{u_r},l}+\tilde{z}_{m_{u_t},q_{u_r},p,n},\\ m_{u_t}\in&\left((u_t-1)M,u_tM-1\right),u_t=1,2,\cdots,U_T,\\ q_{u_r}\in&\left((u_r-1)Q,u_rQ-1\right),u_r=1,2,\cdots,U_R,\\ p=&0,1,\cdots,P-1,\\ n=&0,1,\cdots,N-1,\end{aligned}\tag{20}$$

where $\tilde{\beta}_l=\beta_l/\tilde{s}_{m_{u_t},n,p}$ and $\tilde{z}_{m_{u_t},q_{u_r},p,n}=z_{m_{u_t},q_{u_r},p,n}/\tilde{s}_{m_{u_t},n,p}$.

To better illustrate our method, we construct the tensor using the noiseless item $\tilde{y}_{m_{u_t},q_{u_r},p,n}$, i.e., letting

$$\tilde{x}_{m_{u_t},q_{u_r},p,n}=\sum_{l=1}^{L}\tilde{\beta}_l \mathrm{e}^{-\mathrm{j}2\pi n\Delta f\tau_{M_T/2,Q_R/2,l}}\mathrm{e}^{\mathrm{j}2\pi f_c\left(\frac{2v_l^{u_t,u_t}pT_0}{c}\right)}\gamma_{m_{u_t},q_{u_r},l}.\tag{21}$$

To obtain a tensor that admits a CP decomposition, let

$$\tilde{m}_{u_t,u_r}=\left(m_{u_t}-(u_t-1)M\right)Q+q_{u_r}-(u_r-1)Q,\tag{22}$$

and rearrange $\gamma_{m_{u_t},q_{u_r},l}$ to form $\gamma_{\tilde{m}_{u_t,u_r},l}$. Moreover, samples $\tilde{x}_{m_{u_t},q_{u_r},p,n}$ are rearranged to form a third-order tensor $\boldsymbol{\mathcal{X}}_{u_t,u_r}\in\mathbb{C}^{N\times P\times MQ}$, whose three modes stand for the sub-carrier, the OFDM symbol, and the transceiver antenna pairs, respectively, i.e.,

$$\boldsymbol{\mathcal{X}}_{u_t,u_r}=\sum_{l=1}^{L}\tilde{\beta}_l\boldsymbol{a}_{u_t,u_r,l}\circ\boldsymbol{b}_{u_t,u_r,l}\circ\boldsymbol{c}_{u_t,u_r,l},\tag{23}$$

where

$$a_{u_t,u_r,l}(n)=\mathrm{e}^{-\mathrm{j}2\pi n\Delta f\tau_{M_T/2,Q_R/2,l}},n=0,1,\cdots,N-1,\tag{24}$$

$$b_{u_t,u_r,l}(p)=\mathrm{e}^{\mathrm{j}2\pi f_c\left(\frac{2v_l^{u_t,u_t}pT_0}{c}\right)},p=0,1,\cdots,P-1,\tag{25}$$

$$c_{u_t,u_r,l}\left(\tilde{m}_{u_t,u_r}\right)=\gamma_{\tilde{m}_{u_t,u_r},l},\tilde{m}_{u_t,u_r}=0,1,\cdots,MQ.\tag{26}$$

When only the observations $\{\tilde{y}_{m_{u_t},q_{u_r},p,n}\}$ are available, we can readily construct an incomplete third-order tensor $\boldsymbol{\mathcal{Y}}_{u_t,u_r}$ using the manner in which $\boldsymbol{\mathcal{X}}_{u_t,u_r}$ is constructed. Because the number of targets L is known a priori, the CP decomposition of $\boldsymbol{\mathcal{Y}}_{u_t,u_r}$ can be accomplished by solving the optimization problem (27):

$$\begin{aligned}&\min_{\hat{\boldsymbol{a}}_{u_t,u_r,l},\hat{\boldsymbol{b}}_{u_t,u_r,l},\hat{\boldsymbol{c}}_{u_t,u_r,l}}\left\|\boldsymbol{\mathcal{Y}}_{u_t,u_r}-\boldsymbol{\mathcal{X}}_{u_t,u_r}\right\|_F^2\Leftrightarrow\\&\min_{\hat{\boldsymbol{a}}_{u_t,u_r,l},\hat{\boldsymbol{b}}_{u_t,u_r,l},\hat{\boldsymbol{c}}_{u_t,u_r,l}}\left\|\boldsymbol{\mathcal{Y}}_{u_t,u_r}-\sum_{l=1}^{L}\tilde{\beta}_l\boldsymbol{a}_{u_t,u_r,l}\circ\boldsymbol{b}_{u_t,u_r,l}\circ\boldsymbol{c}_{u_t,u_r,l}\right\|_F^2.\end{aligned}\tag{27}$$

According to Chen HY et al. (2021) and Li et al. (2023), we have the conclusions in Lemma 1.

Lemma 1 Let $\boldsymbol{\mathcal{A}}\in\mathbb{C}^{I_1\times I_2\times\cdots\times I_M}$ denote an M^{th}-order tensor with $(i_1, i_2, \cdots, i_M)^{\text{th}}$ entry denoted as $\mathcal{A}_{i_1,i_2,\cdots,i_M}$. Here, the order M of a tensor is the number of dimensions. The CP decomposition decomposes a tensor into a sum of rank-one component tensors, i.e.,

$$\boldsymbol{\mathcal{A}}=\sum_{l=1}^{L_0}\boldsymbol{x}_l^1\circ\boldsymbol{x}_l^2\circ\cdots\circ\boldsymbol{x}_l^M,$$

where $\boldsymbol{x}_l^m\in\mathbb{C}^{I_m}$, $m\in\{1,2,\cdots,M\}$. The minimum achievable L_0 is referred to as the rank of the tensor, and $\boldsymbol{X}^m=[\boldsymbol{x}_1^m,\boldsymbol{x}_2^m,\cdots,\boldsymbol{x}_{L_0}^m]\in\mathbb{C}^{I_m\times L_0}$ denotes the factor along the m^{th} mode. When the Kruskal condition holds true, i.e.,

$$\begin{aligned}&\min(I_1,L_0)+\min(I_2,L_0)\\&\quad+\cdots+\min(I_M,L_0)\geq 2L_0+2,\end{aligned}$$

the CP decomposition is unique.

Applying the above Lemma 1 to Eq. (27), the tensor $\boldsymbol{\mathcal{Y}}_{u_t,u_r}\in\mathbb{C}^{N\times P\times MQ}$ can be decomposed into a sum of rank-one component tensors $\hat{\boldsymbol{a}}_{u_t,u_r,l}$, $\hat{\boldsymbol{b}}_{u_t,u_r,l}$, $\hat{\boldsymbol{c}}_{u_t,u_r,l}$ ($l=1,2,\cdots,L$; $u_t=1,2,\cdots,U_T$; $u_r=1,2,\cdots,U_R$).

Moreover, because P, N, and MQ are greater than L, the Kruskal condition holds true when $L\geq 2$. Additionally, De Lathauwer (2006) demonstrated that for the case $L=1$, the CP decomposition held true. Therefore, as long as P, N, and MQ are greater than L, the above CP decomposition given by Lemma 1 is unique.

3.2 Parameter estimation

We now discuss how to estimate the parameters $\{(x_l,y_l)\}$ and $\{(v_{x,l},v_{y,l})\}$ based on the estimated factor matrices composed of $\hat{\boldsymbol{a}}_{u_t,u_r,l}$, $\hat{\boldsymbol{b}}_{u_t,u_r,l}$, $\hat{\boldsymbol{c}}_{u_t,u_r,l}$.

$\boldsymbol{a}_{u_t,u_r,l}$ is characterized by $\tau_{M_T/2,Q_R/2,l}$, which can be estimated via reformulating Eq. (24) and using a simple averaging method over n, giving as

$$\hat{\tau}_{M_T/2,Q_R/2,l}=\frac{1}{2\pi\Delta f(N-1)U_TU_R}\sum_{u_t=1}^{U_T}\sum_{u_r=1}^{U_R}\sum_{n=0}^{N-2}\angle\left(\frac{\hat{a}_{u_t,u_r,l}(n)}{\hat{a}_{u_t,u_r,l}(n+1)}\right).\quad(28)$$

Similarly, $\boldsymbol{b}_{u_t,u_r,l}$ is characterized by $v_l^{u_t,u_r}$, which can be estimated by reformulating Eq. (25) and using a simple averaging method over p, giving as

$$\hat{v}_l^{u_t,u_r}=\frac{c}{4\pi f_cT_0(P-1)}\sum_p\angle\left(\frac{\hat{b}_{u_t,u_r,l}(p)}{\hat{b}_{u_t,u_r,l}(p+1)}\right).\quad(29)$$

$\boldsymbol{c}_{u_t,u_r,l}$ is characterized by $\delta^R_{q_{u_t},l}$, which can be estimated by combining Eqs. (26) and (19), and using a simple averaging method over $\tilde{m}_{u_t,u_r}$, giving as

$$\hat{\delta}^R_{q_{u_t},l}=\frac{c}{2\pi K\Delta fM_T}\sum_{u_t=1}^{U_T}\sum_{m_{u_t}=1}^{M}\angle\left(\frac{\hat{\gamma}_{m_{u_t},q_{u_t},l}}{\hat{\gamma}_{m_{u_t},Q_R/2,l}}\Big/\frac{\hat{\gamma}_{m_{u_t}-1,q_{u_t},l}}{\hat{\gamma}_{m_{u_t}-1,Q_R/2,l}}\right),\quad(30)$$

where $\hat{\gamma}_{m_{u_t},q_{u_t},l}=\hat{c}_{u_t,u_r,l}(\tilde{m}_{u_t,u_r})$.

3.2.1 Estimation of $\{(x_l,y_l)\}$

By the definition of $\delta^R_{q_{u_t},l}$ and $\tau_{M_T/2,Q_R/2,l}$ in Eqs. (7) and (10), respectively, these parameters are related to $\{x_l,y_l\}$. Inspired by these observations, we focus on solving $\{x_l,y_l\}$.

Rearranging the formulas in Eq. (7), we arrive at

$$\left(\delta^R_{q_{u_t},l}+\rho^R_{Q_R/2,l}\right)^2=x_l^2+y_l^2+x^2_{R,q_{u_t}}-2x_{R,q_{u_t}}x_l,\quad(31)$$

which, combined with Eq. (9), indicates that

$$\begin{aligned}&2\left(x_{R,q_{u_t}}-x_{R,Q_R/2}\right)x_l+2\delta^R_{q_{u_t},l}\rho^R_{Q_R/2,l}\\&=x^2_{R,q_{u_t}}-x^2_{R,Q_R/2}-(\delta^R_{q_{u_t},l})^2,\end{aligned}\quad(32)$$

where $q_{u_t}\in\left((u_r-1)Q,u_rQ-1\right)$, $u_r=1,2,\cdots,U_R$. Therefore, we have several Q_R equations based on Eq. (32). Reformulating those equations as a vector, we have

$$\boldsymbol{P}\boldsymbol{w}_l=\boldsymbol{h}_l,\quad(33)$$

where

$$\begin{aligned}&\boldsymbol{P}\triangleq 2\begin{bmatrix}x_{R,0}-x_{R,Q_R/2}&\delta^R_{0,l}\\x_{R,1}-x_{R,Q_R/2}&\delta^R_{1,l}\\\vdots&\vdots\\x_{R,Q_R-1}-x_{R,Q_R/2}&\delta^R_{Q_R-1,l}\end{bmatrix},\boldsymbol{w}_l\triangleq\begin{bmatrix}x_l\\\rho^R_{Q_R/2,l}\end{bmatrix},\\&\boldsymbol{h}_l\triangleq\begin{bmatrix}x^2_{R,0}-x^2_{R,Q_R/2}-\left(\delta^R_{0,l}\right)^2\\x^2_{R,1}-x^2_{R,Q_R/2}-\left(\delta^R_{1,l}\right)^2\\\vdots\\x^2_{R,Q_R-1}-x^2_{R,Q_R/2}-\left(\delta^R_{Q_R-1,l}\right)^2\end{bmatrix}.\end{aligned}\quad(34)$$

The combination of Eqs. (8) and (9) indicates that

$$\rho^T_{M_T/2,l}=\sqrt{(\rho^R_{Q_R/2,l})^2+2x_l(x_{R,Q_R/2}-x_{T,M_T/2})}.\quad(35)$$

Substituting $\rho^T_{M_T/2,l}$ in Eq. (35) into Eq. (10), we obtain

$$\rho^{\mathrm{R}}_{Q_{\mathrm{R}}/2,l}+\sqrt{(\rho^{\mathrm{R}}_{Q_{\mathrm{R}}/2,l})^2+2\xi x_l}=c\tau_{M_{\mathrm{T}}/2,Q_{\mathrm{R}}/2,l}, \quad (36)$$

where $\xi\triangleq x_{\mathrm{R},Q_{\mathrm{R}}/2}-x_{\mathrm{T},M_{\mathrm{T}}/2}$.

If the estimations of $\hat{\delta}^{\mathrm{r}}_{q,l}$ and $\hat{\tau}_{M_{\mathrm{T}}/2,Q_{\mathrm{R}}/2,l}$ are perfect, substituting them into Eqs. (33) and (36) and solving the resulting equations, we can obtain the variables x_l and $\rho^{\mathrm{R}}_{Q_{\mathrm{R}}/2,l}$. However, due to the estimation error of $\hat{\delta}^{\mathrm{r}}_{q,l}$ and $\hat{\tau}_{M_{\mathrm{T}}/2,Q_{\mathrm{R}}/2,l}$, the resulting equations may not hold true. As such, we optimize the square error with respect to x_l and $\rho^{\mathrm{R}}_{Q_{\mathrm{R}}/2,l}$.

$$\begin{aligned}&\min_{\hat{x}_l,\hat{\rho}^{\mathrm{R}}_{Q_{\mathrm{R}}/2,l}}\left\|\hat{\boldsymbol{P}}\boldsymbol{w}_l-\hat{\boldsymbol{h}}_l\right\|_{\mathrm{F}}^2+\left|c\hat{\tau}_{M_{\mathrm{T}}/2,Q_{\mathrm{R}}/2,l}\right.\\&\left.-\sqrt{\left(\rho^{\mathrm{R}}_{Q_{\mathrm{R}}/2,l}\right)^2+2\xi x_l}-\rho^{\mathrm{R}}_{Q_{\mathrm{R}}/2,l}\right|^2\\&\text{s.t.}\ \rho^{\mathrm{R}}_{Q_{\mathrm{R}}/2,l}\geq\left|x_l-x_{\mathrm{R},Q_{\mathrm{R}}/2}\right|,\end{aligned} \quad (37)$$

where $\hat{\boldsymbol{P}}$ and $\hat{\boldsymbol{h}}_l$ are obtained by substituting $\hat{\delta}^{\mathrm{r}}_{q,l}$ and $\hat{\tau}_{M_{\mathrm{T}}/2,Q_{\mathrm{R}}/2,l}$ into Eqs. (33) and (36), respectively.

The above optimization problem is non-convex due to the nonlinear item $\sqrt{\left(\rho^{\mathrm{R}}_{Q_{\mathrm{R}}/2,l}\right)^2+2\xi x_l}$. In the following, our key approach for solving this problem is to perform Taylor expansion on that item, to transform the optimization problem into a convex one. To that end, we first need to know a rough estimation of x_l and $\rho^{\mathrm{R}}_{Q_{\mathrm{R}}/2,l}$, which is given by Lemma 2.

Lemma 2 Let θ_l be the azimuth of the target relative to the $(Q_{\mathrm{R}}/2)^{\mathrm{th}}$ receiving antenna, as shown in Fig. 2. Combining Eqs. (33) and (36), we arrive at

$$\begin{aligned}&\check{\rho}^{\mathrm{R}}_{Q_{\mathrm{R}}/2,l}=\frac{\left(c\hat{\tau}_{M_{\mathrm{T}}/2,Q_{\mathrm{R}}/2,l}\right)^2+2\xi^2}{2c\hat{\tau}_{M_{\mathrm{T}}/2,Q_{\mathrm{R}}/2,l}-2\cos\hat{\theta}_l\xi},\\&\check{x}_l=\check{\rho}^{\mathrm{R}}_{Q_{\mathrm{R}}/2,l}\cos\hat{\theta}_l+x_{\mathrm{R},Q_{\mathrm{R}}/2}.\end{aligned}$$

The proof is given in the Appendix.

Performing a Taylor expansion of $\sqrt{(\rho^{\mathrm{R}}_{Q_{\mathrm{R}}/2,l})^2+2\xi x_l}$ near the point $\left(\check{x}_l,\check{\rho}^{\mathrm{R}}_{Q_{\mathrm{R}}/2,l}\right)$, we obtain

$$\begin{aligned}&\sqrt{(\rho^{\mathrm{R}}_{Q_{\mathrm{R}}/2,l})^2+2\xi x_l}=\sqrt{(\check{\rho}^{\mathrm{R}}_{Q_{\mathrm{R}}/2,l})^2+2\check{x}_l\xi}\\&+\frac{\check{\rho}^{\mathrm{R}}_{Q_{\mathrm{R}}/2,l}}{\sqrt{(\check{\rho}^{\mathrm{R}}_{Q_{\mathrm{R}}/2,l})^2+2\check{x}_l\xi}}\left(\rho^{\mathrm{R}}_{Q_{\mathrm{R}}/2,l}-\check{\rho}^{\mathrm{R}}_{Q_{\mathrm{R}}/2,l}\right)\\&+\frac{\xi}{\sqrt{(\check{\rho}^{\mathrm{R}}_{Q_{\mathrm{R}}/2,l})^2+2\check{x}_l\xi}}\left(x_l-\check{x}_l\right).\end{aligned} \quad (38)$$

Substituting $\check{x}_l$ and $\check{\rho}^{R}_{Q_R/2,l}$ into Eq. (36), we obtain

$$\check{\rho}^{\mathrm{R}}_{Q_{\mathrm{R}}/2,l}=c\hat{\tau}_{M_{\mathrm{T}}/2,Q_{\mathrm{R}}/2,l}-\sqrt{(\check{\rho}^{\mathrm{R}}_{Q_{\mathrm{R}}/2,l})^2+2\check{x}_l\xi}. \quad (39)$$

The combination of Eqs. (38) and (39) can obtain

$$\begin{aligned}&\left|c\hat{\tau}_{M_{\mathrm{T}}/2,Q_{\mathrm{R}}/2,l}-\sqrt{(\rho^{\mathrm{R}}_{Q_{\mathrm{R}}/2,l})^2+2x_l\xi}-\rho^{\mathrm{R}}_{Q_{\mathrm{R}}/2,l}\right|^2\\&=\left|\hat{\rho}^{\mathrm{R}}_{Q_{\mathrm{R}}/2,l}-\frac{\check{\rho}^{\mathrm{R}}_{Q_{\mathrm{R}}/2,l}}{\sqrt{(\check{\rho}^{\mathrm{R}}_{Q_{\mathrm{R}}/2,l})^2+2\check{x}_l\xi}}\left(\rho^{\mathrm{R}}_{Q_{\mathrm{R}}/2,l}-\check{\rho}^{\mathrm{R}}_{Q_{\mathrm{R}}/2,l}\right)\right.\\&\left.-\frac{\check{x}_l\xi}{\sqrt{(\check{\rho}^{\mathrm{R}}_{Q_{\mathrm{R}}/2,l})^2+2\check{x}_l\xi}}\left(x_l-\check{x}_l\right)-\rho^{\mathrm{R}}_{Q_{\mathrm{R}}/2,l}\right|^2\\&=\left|\check{\rho}^{\mathrm{R}}_{Q_{\mathrm{R}}/2,l}+\frac{(\check{\rho}^{\mathrm{R}}_{Q_{\mathrm{R}}/2,l})^2+\check{x}_l^2\xi}{\sqrt{(\check{\rho}^{\mathrm{R}}_{Q_{\mathrm{R}}/2,l})^2+2\check{x}_l\xi}}\right.\\&-\left(1+\frac{\check{\rho}^{\mathrm{R}}_{Q_{\mathrm{R}}/2,l}}{\sqrt{(\check{\rho}^{\mathrm{R}}_{Q_{\mathrm{R}}/2,l})^2+2\check{x}_l\xi}}\right)\rho^{\mathrm{R}}_{Q_{\mathrm{R}}/2,l}\\&\left.-\frac{\check{x}_l\xi}{\sqrt{(\check{\rho}^{\mathrm{R}}_{Q_{\mathrm{R}}/2,l})^2+2\check{x}_l\xi}}x_l\right|^2.\end{aligned} \quad (40)$$

Substituting Eq. (40) into the optimization problem (37), we transform Eq. (37) into a convex optimization problem as follows:

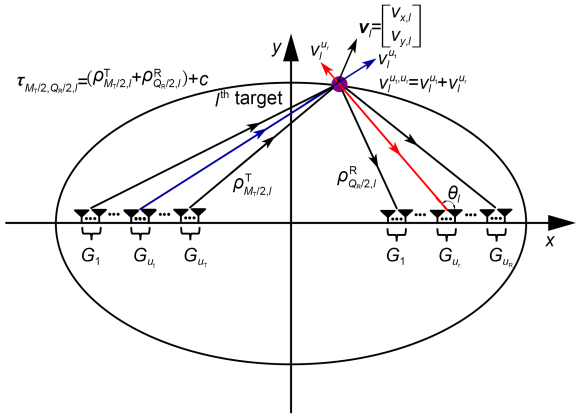

Fig. 2 Illustration of the rough estimation model. The target is located on an ellipse, which is determined by $\hat{\tau}_l$, and the two focal points of the ellipse are the $(M_{\mathrm{T}}/2)^{\mathrm{th}}$ transmitting antenna and the $(Q_{\mathrm{R}}/2)^{\mathrm{th}}$ receiving antenna. The position of the target is at the intersection of the ellipse and the azimuth θ_l

$$\min_{\hat{x}_l,\hat{\rho}^{\mathrm{R}}_{Q_{\mathrm{R}}/2,l}} \left\| \boldsymbol{P}'\boldsymbol{w}_l-\boldsymbol{h}'_l \right\|^2 \quad \text{s.t. } \rho^{\mathrm{R}}_{Q_{\mathrm{R}}/2,l}\geq\left| x_l-x_{\mathrm{R},Q_{\mathrm{R}}/2} \right|, \tag{41}$$

where

$$\boldsymbol{P}'=\begin{bmatrix} \hat{\boldsymbol{P}} \\ \dfrac{\check{x}_l\xi}{\sqrt{(\check{\rho}^{\mathrm{R}}_{Q_{\mathrm{R}}/2,l})^2+2\check{x}_l\xi}} & 1+\dfrac{\check{\rho}^{\mathrm{R}}_{Q_{\mathrm{R}}/2,l}}{\sqrt{(\check{\rho}^{\mathrm{R}}_{Q_{\mathrm{R}}/2,l})^2+2\check{x}_l\xi}} \end{bmatrix},$$

$$\boldsymbol{h}'_l=\begin{bmatrix} \hat{\boldsymbol{h}}_l \\ \check{\rho}^{\mathrm{R}}_{Q_{\mathrm{R}}/2,l}+\dfrac{(\check{\rho}^{\mathrm{R}}_{Q_{\mathrm{R}}/2,l})^2+\check{x}_l^2\xi}{\sqrt{(\check{\rho}^{\mathrm{R}}_{Q_{\mathrm{R}}/2,l})^2+2\check{x}_l\xi}} \end{bmatrix}.$$

The optimization problem is convex, where $\check{x}_l$ and $\check{\rho}^{\mathrm{R}}_{Q_{\mathrm{R}}/2,l}$ can be obtained using the CVX toolbox. Substituting $\check{x}_l$ and $\check{\rho}^{\mathrm{R}}_{Q_{\mathrm{R}}/2,l}$ into Eq. (9), we obtain

$$\hat{y}_l=\sqrt{(\hat{\rho}^{\mathrm{R}}_{Q_{\mathrm{R}}/2,l})^2-(\hat{x}_l-x_{\mathrm{R},Q_{\mathrm{R}}/2})^2}. \tag{42}$$

This completes the estimation of $\{(x_l, y_l)\}$.

3.2.2 Estimation of $\{(v_{x,l}, v_{y,l})\}$

In the near field, the observed velocity differs for different groups of transceiver antennas, as estimated in Eq. (29). This observed velocity is related not only to the target's velocity $\{(v_{x,l}, v_{y,l})\}$, but also to the target's position (x_l, y_l). In this subsection, we give details for obtaining $\{(v_{x,l}, v_{y,l})\}$ based on $\hat{v}_l^{u_{\mathrm{t}},u_{\mathrm{r}}}$ and $\{(\hat{x}_l,\hat{y}_l)\}$.

As shown in Fig. 2, the velocity $v_l^{u_{\mathrm{t}},u_{\mathrm{r}}}$ consists of two parts: $v_l^{u_{\mathrm{t}},u_{\mathrm{r}}}=v_l^{u_{\mathrm{t}}}+v_l^{u_{\mathrm{r}}}$, where $v_l^{u_{\mathrm{t}}}$ and $v_l^{u_{\mathrm{r}}}$ are the radial velocities relative to the transmitting and receiving sub-arrays, respectively. According to the geometric information, $v_l^{u_{\mathrm{t}}}$ and $v_l^{u_{\mathrm{r}}}$ can be rewritten as

$$v_l^{u_{\mathrm{t}}}=\frac{v_{x,l}\left(x_{\mathrm{T},\left(u_{\mathrm{t}}-\frac{1}{2}\right)M}-x_l\right)-v_{y,l}y_l}{\rho^{\mathrm{T}}_{\left(u_{\mathrm{t}}-\frac{1}{2}\right)M,l}}, \tag{43}$$

$$v_l^{u_{\mathrm{r}}}=\frac{v_{x,l}\left(x_{\mathrm{R},\left(u_{\mathrm{r}}-\frac{1}{2}\right)Q}-x_l\right)-v_{y,l}y_l}{\rho^{\mathrm{R}}_{\left(u_{\mathrm{r}}-\frac{1}{2}\right)Q,l}}, \tag{44}$$

and $\left(x_{\mathrm{T},\left(u_{\mathrm{t}}-\frac{1}{2}\right)M},0\right)$ and $\left(x_{\mathrm{R},\left(u_{\mathrm{r}}-\frac{1}{2}\right)Q},0\right)$ are the location of the center antenna of the $u_{\mathrm{t}}^{\mathrm{th}}$ transmit sub-array and $u_{\mathrm{r}}^{\mathrm{th}}$ receive sub-array, respectively. Therefore, $v_l^{u_{\mathrm{t}},u_{\mathrm{r}}}$ can be rewritten as

$$v_l^{u_{\mathrm{t}},u_{\mathrm{r}}}=\begin{bmatrix} \dfrac{x_{\mathrm{T},\left(u_{\mathrm{t}}-\frac{1}{2}\right)M}-x_l}{\rho^{\mathrm{T}}_{\left(u_{\mathrm{t}}-\frac{1}{2}\right)M,l}}+\dfrac{x_{\mathrm{R},\left(u_{\mathrm{r}}-\frac{1}{2}\right)Q}-x_l}{\rho^{\mathrm{R}}_{\left(u_{\mathrm{r}}-\frac{1}{2}\right)Q,l}}, \\ \dfrac{-y_l}{\rho^{\mathrm{T}}_{\left(u_{\mathrm{t}}-\frac{1}{2}\right)M,l}}+\dfrac{-y_l}{\rho^{\mathrm{R}}_{\left(u_{\mathrm{r}}-\frac{1}{2}\right)Q,l}} \end{bmatrix}\begin{bmatrix} v_{x,l} \\ v_{y,l} \end{bmatrix}, \tag{45}$$

$$u_{\mathrm{t}}=1,2,\cdots,U_{\mathrm{T}},\ u_{\mathrm{r}}=1,2,\cdots,U_{\mathrm{R}}.$$

Let $\hat{\boldsymbol{v}}_l\triangleq\left[\hat{v}_l^{1,1},\cdots,\hat{v}_l^{u_{\mathrm{t}},u_{\mathrm{r}}},\cdots,\hat{v}_l^{U_{\mathrm{T}},U_{\mathrm{R}}}\right]^{\mathrm{T}}$, where $\hat{v}_l^{u_{\mathrm{t}},u_{\mathrm{r}}}$ ($u_{\mathrm{t}}=1,2,\cdots,U_{\mathrm{T}}$; $u_{\mathrm{r}}=1,2,\cdots,U_{\mathrm{R}}$) are obtained using Eq. (29). Substituting $\hat{v}_l^{u_{\mathrm{t}},u_{\mathrm{r}}}$ and $\left(\hat{x}_l,\hat{y}_l\right)$ into Eq. (45), we obtain several $U_{\mathrm{T}}U_{\mathrm{R}}$ equations, which can be rewritten as

$$\hat{\boldsymbol{v}}_l=\boldsymbol{G}\begin{bmatrix} \hat{v}_{x,l} \\ \hat{v}_{y,l} \end{bmatrix}, \tag{46}$$

where

$$\boldsymbol{G}\triangleq\begin{bmatrix} \dfrac{x_{\mathrm{T},\frac{M}{2}}-\hat{x}_l}{\rho^{\mathrm{T}}_{\frac{M}{2},L}}+\dfrac{x_{\mathrm{R},\frac{Q}{2}}-\hat{x}_l}{\rho^{\mathrm{R}}_{\frac{Q}{2},l}} & \dfrac{-\hat{y}_l}{\rho^{\mathrm{T}}_{\frac{M}{2},L}}+\dfrac{-\hat{y}_l}{\rho^{\mathrm{R}}_{\frac{Q}{2},l}} \\ \vdots & \vdots \\ \dfrac{x_{\mathrm{T},\left(U_{\mathrm{T}}-\frac{1}{2}\right)M}-\hat{x}_l}{\rho^{\mathrm{T}}_{\left(U_{\mathrm{T}}-\frac{1}{2}\right)M,l}}+\dfrac{x_{\mathrm{R},\left(U_{\mathrm{R}}-\frac{1}{2}\right)Q}-\hat{x}_l}{\rho^{\mathrm{R}}_{\left(U_{\mathrm{R}}-\frac{1}{2}\right)Q,l}} & \dfrac{-\hat{y}_l}{\rho^{\mathrm{T}}_{\left(U_{\mathrm{T}}-\frac{1}{2}\right)M,l}}+\dfrac{-\hat{y}_l}{\rho^{\mathrm{R}}_{\left(U_{\mathrm{R}}-\frac{1}{2}\right)Q,l}} \end{bmatrix}.$$

Finally, $\hat{v}_{x,l}$ and $\hat{v}_{y,l}$ can be estimated by the least square (LS) algorithm

$$\begin{bmatrix} \hat{v}_{x,l} \\ \hat{v}_{y,l} \end{bmatrix}=\left(\boldsymbol{G}^{\mathrm{T}}\boldsymbol{G}\right)^{-1}\boldsymbol{G}^{\mathrm{T}}\hat{\boldsymbol{v}}_l. \tag{47}$$

The algorithm discussed above provides a method of target localization and velocity estimation based on the estimated parameters at tensor decomposition. To improve the localization accuracy, an optimization problem is constructed by combining parameters $\hat{\tau}_{M_{\mathrm{T}}/2,Q_{\mathrm{R}}/2,l}$ and $\hat{\delta}^{\mathrm{R}}_{q_{u_{\mathrm{r}}},l}$ under the minimum variance criterion. Then, the target velocity is estimated using the estimated target position and $\hat{v}_l^{u_{\mathrm{t}},u_{\mathrm{r}}}$. To summarize, the proposed CP-NFL algorithm is presented as Algorithm 1.

Algorithm 1 CP-NFL algorithm

Input: array groupings U_{T} and U_{R}, tensors of receiving data $\boldsymbol{\mathcal{Y}}_1, \boldsymbol{\mathcal{Y}}_2 \cdots, \boldsymbol{\mathcal{Y}}_{U_{\mathrm{R}}U_{\mathrm{T}}}$, and target number L.

Output: position $\left(\hat{x}_l, \hat{y}_l\right)$ and velocity $(\hat{v}_{x,l}, \hat{v}_{y,l})$, where l=1, 2, ···, L.

for $u_{\mathrm{t}} = 1{:}U_{\mathrm{T}}$ **do**
  for $u_{\mathrm{r}} = 1{:}U_{\mathrm{R}}$ **do**
    Tensor decomposition of $\boldsymbol{\mathcal{Y}}_{u_{\mathrm{t}}u_{\mathrm{r}}}$
    yielding $\hat{\boldsymbol{a}}_{u_{\mathrm{t}},u_{\mathrm{r}},l}, \hat{\boldsymbol{b}}_{u_{\mathrm{t}},u_{\mathrm{r}},l}, \hat{\boldsymbol{c}}_{u_{\mathrm{t}},u_{\mathrm{r}},l}$
  end for
end for
for $l = 1{:}L$ **do**
  Compute $\hat{\tau}_{M_{\mathrm{T}}/2,Q_{\mathrm{R}}/2,l}$, $\hat{v}_l^{u_{\mathrm{t}},u_{\mathrm{r}}}$, and $\hat{\delta}^{\mathrm{R}}_{q_{u_{\mathrm{r}}},l}$ using Eqs. (28)–(30)
  Compute $\check{x}_l$ and $\check{\rho}^{\mathrm{R}}_{Q_{\mathrm{R}}/2,l}$ by Lemma 2
  Estimate $\left(\hat{x}_l, \hat{\rho}^{\mathrm{R}}_{Q_{\mathrm{R}}/2,l}\right)$ by solving the optimization problem (41) with the CVX tool
  Compute the position parameter $\hat{x}_l$ using Eq. (42)
  Compute the velocity $\left(\hat{v}_{x,l}, \hat{v}_{y,l}\right)$ using Eq. (47)
end for

3.3 Computational complexity analysis

The computational complexity of the significant steps in the CP-NFL algorithm includes CP decomposition, estimation of $\hat{\tau}_{M_{\mathrm{T}}/2,Q_{\mathrm{R}}/2,l}$, $\hat{v}_l^{u_{\mathrm{t}},u_{\mathrm{r}}}$, and $\hat{\delta}^{\mathrm{R}}_{q_{u_{\mathrm{r}}},l}$, and solving the optimization problem in Eq. (45). The computational complexity of tensor decomposition for each group of received data is (Da Rosa Zanatta et al., 2019)

$$\mathcal{O}(\mathrm{CPD}) = \mathcal{O}\Big(P^3 + N^3 + (\mathrm{MQ})^3 + L^3 + L(\mathrm{MQ})N^2 + L(\mathrm{MQ})^2 N + L^2 PN(\mathrm{MQ})\Big).$$

The computational complexity of estimating $\hat{\tau}_{M_{\mathrm{T}}/2,Q_{\mathrm{R}}/2,l}$, $\hat{v}_l^{u_{\mathrm{t}},u_{\mathrm{r}}}$, $\hat{\delta}^{\mathrm{R}}_{q_{u_{\mathrm{r}}},l}$ is $\mathcal{O}(L(\mathrm{MQ}))$ for each group. The computational complexity of localization by solving the optimization problem is $\mathcal{O}(T)$, where T is the number of iterations. Because there are $U_{\mathrm{T}}U_{\mathrm{R}}$ groups, the total computational complexity is $U_{\mathrm{T}}U_{\mathrm{R}}(\mathcal{O}(\mathrm{CPD})+\mathcal{O}(L(\mathrm{MQ})))+\mathcal{O}(T)$. Meanwhile, $\mathcal{O}(L(\mathrm{MQ}))$ can be ignored when it is compared to $\mathcal{O}(\mathrm{CPD})$. Finally, we can obtain

$$\begin{aligned}\mathcal{O}(\mathrm{CP\text{-}NFL}) &= U_{\mathrm{T}}U_{\mathrm{R}}\left(\mathcal{O}(\mathrm{CPD})\right)+\mathcal{O}(T)\\ &= \mathcal{O}\Bigg(U_{\mathrm{T}}U_{\mathrm{R}}\left(P^3+N^3+L^3\right)\\ &\quad +\frac{\left(M_{\mathrm{T}}Q_{\mathrm{R}}\right)^3}{\left(U_{\mathrm{T}}U_{\mathrm{R}}\right)^2}+L\frac{\left(M_{\mathrm{T}}Q_{\mathrm{R}}\right)^2}{U_{\mathrm{T}}U_{\mathrm{R}}}N\Bigg)\\ &\quad +\mathcal{O}(LM_{\mathrm{T}}Q_{\mathrm{R}}N^2+L^2PNM_{\mathrm{T}}Q_{\mathrm{R}})+\mathcal{O}(T).\end{aligned} \tag{48}$$

The computational complexity varies with the number of groups. When $M_{\mathrm{T}}Q_{\mathrm{R}}$ is larger than Q, P, and N, appropriately increasing the number of groups can reduce the complexity caused by the number of antennas, and thus reduce the overall complexity.

4 Numerical results

This section presents numerical results to validate the proposed schemes. In the simulation, the carrier frequency is set to f_{c}=300 GHz, resulting in the wavelength $\lambda=c/f_{\mathrm{c}}$=1 mm, and the sub-carrier spacing is Δf=300 kHz, giving an OFDM symbol duration of $T_0=1/\Delta f+T_{\mathrm{CP}}=1.25/\Delta f\approx 4.1667$ μs. The distance between the origin of the coordinate and 0$^{\mathrm{th}}$ transmit or receive antenna is d'=0.2 m, and the antenna element spacing is $d=10\lambda$=1 cm, so the total size of the receiving array is $D_{\mathrm{R}}=(Q_{\mathrm{R}}-1)d$=0.29 m. Assume that the parameter estimation is carried out over a frame of P=60 OFDM symbols, with K=401. We assume that the target is located within the area $\theta\in[-90°, 90°]$ in elevation and $r\in$[1 m, 30 m] in distance. All simulations are performed with K_{T}=1000 trials. Unless otherwise specified, the number of receiving antennas is Q_{R}=30, divided into six groups (U_{R}=6), and the number of transmitting antennas is M_{T}=31, constituting one group (U_{T}=1). The velocity is defined in polar coordinates. Unless otherwise specified, the angle of the velocity is set to 45°. For the scenario with one target, its velocity is set to 0.5 m/s; therefore, the velocities along the Cartesian coordinates are $v_x=0.5/\sqrt{2}$ m/s and $v_y=0.5/\sqrt{2}$ m/s. For the scenario with two targets, the velocities are set to 0.5 m/s and 0.7 m/s, respectively. Meanwhile, the signal-to-noise ratio (SNR), the root mean square error

(RMSE) of localization, and the RMSE of velocity in this study are defined as

$$\mathrm{SNR}=\frac{P_{\mathrm{t}}}{L\sigma^2}\sum_l|\alpha_l|^2, \tag{49}$$

$$\mathrm{RMSE}_{xy}=\mathbb{E}\left(\sum_l\frac{\sqrt{(x_l-\hat{x}_l)^2+(y_l-\hat{y}_l)^2}}{2L}\right), \tag{50}$$

$$\mathrm{RMSE}_{v}=\mathbb{E}\left(\sum_l\frac{\sqrt{(\hat{v}_{x,l}-v_{x,l})^2+(\hat{v}_{y,l}-v_{y,l})^2}}{2L}\right), \tag{51}$$

where P_{t} denotes the transmit power, σ^2 denotes variance of noise, and $\mathbb{E}(\cdot)$ represents averaging. In addition, the bandwidth in the simulation refers to the signal bandwidth of each transmitting antenna and the bandwidth is set to 120 MHz if it is not specified.

Figs. 3 and 4 show the relationships between the RMSE and the distance from target to origin and between the RMSE and SNR of the proposed CP-NFL algorithm, respectively. The CP-NFL algorithm is compared with the near-field LS localization algorithm proposed in Podkurkov et al. (2018). As shown in Fig. 3, the estimation performance of the proposed CP-NFL algorithm is much better than that of the LS algorithm. Overall, the accuracy of the algorithms decreases with increasing distance. However, due to the more delicate use of the signal model based on spherical wavefronts, the performance of the CP-NFL algorithm deteriorates more slowly than that of the LS algorithm. In Fig. 4, we set the target distance at 5 m. The figure shows that with increasing SNR, the estimation performance of both algorithms improves. Meanwhile, the estimation performance by the proposed CP-NFL algorithm is better and improves faster compared with the existing LS algorithm.

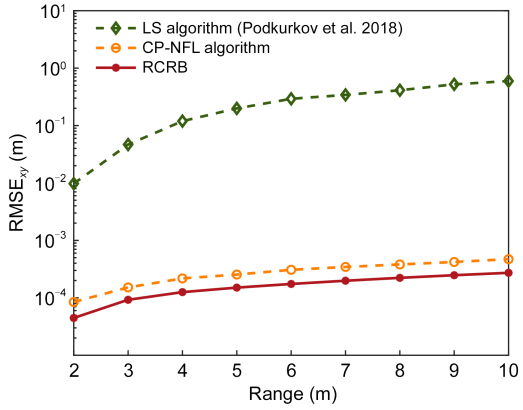

Fig. 3 The RMSE of localization w.r.t. range (distance from target to origin) when the SNR is 15 dB. LS: least square; CP-NFL: CP decomposition-based near-field localization; RCRB: root Crame-Rao bound

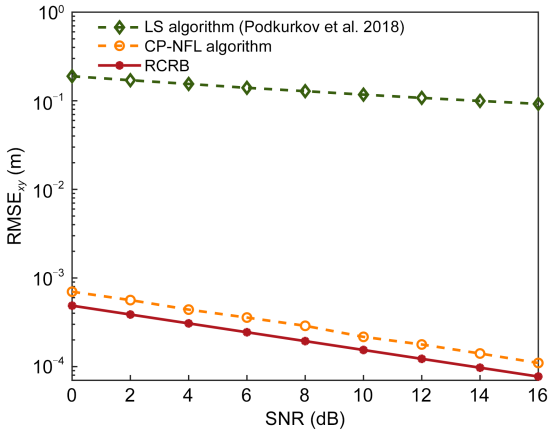

Fig. 4 The RMSE of localization w.r.t. SNR

In Fig. 5, two targets are considered. The distance from the first target to origin (r_1) is set to 10 m, 20 m, 30 m, and 200 m. The x-coordinate denotes the distance between the second target and the first target ($\Delta_{\mathrm{d}}=r_2-r_1$), where r_2 is the distance from the second target to the origin. It can be seen that the estimation accuracy increases as r_1 decreases, due to the more pronounced near-field effect. Moreover, it is more difficult to distinguish the two targets when they are too close, and the estimation accuracy decreases as the distance between the two targets decreases.

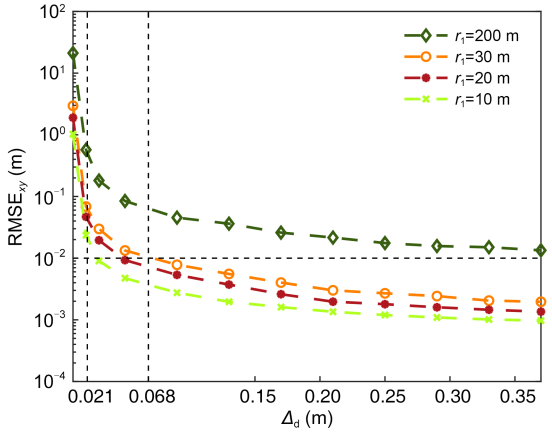

Fig. 5 The RMSE of localization w.r.t. the range between targets with different distances to the first target (SNR=15 dB)

When Δ_d>0.21 m, the estimation accuracy improves slightly with increasing Δ_d, and when Δ_d>0.068 m, the estimation accuracy in the near-field scene can reach the centimeter level. This indicates that when the performance of the CP-NFL algorithm is affected by Δ_d, the estimation accuracy achieves 0.01 m. In Fig. 6, we set the velocities of the two targets to 0.5 m/s and 0.7 m/s, respectively. Because velocity estimation accuracy is affected by position estimation accuracy, the variation trend in velocity estimation follows the same pattern as in Fig. 5.

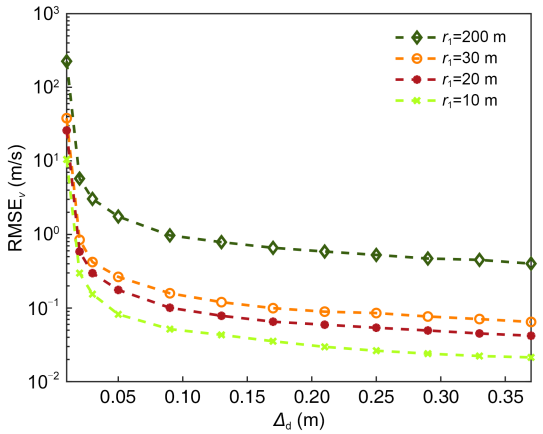

Fig. 6 The RMSE of velocity w.r.t. the range between targets with different distances to the first target (SNR=15 dB)

In Figs. 7 and 8, we set r_1=10 m. The bandwidth varies from 15 MHz to 120 MHz. With the increase in available bandwidth, the estimation accuracy gradually improves, because in this case the estimation of the propagation time delay is more accurate. In addition, when the distance between the two targets is

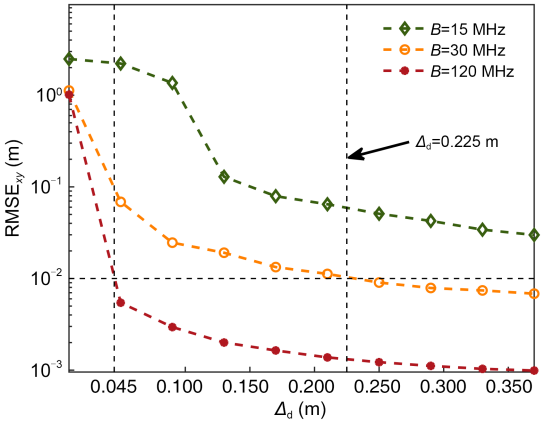

Fig. 7 RMSE of localization w.r.t. the range between targets with different bandwidths (SNR=15 dB)

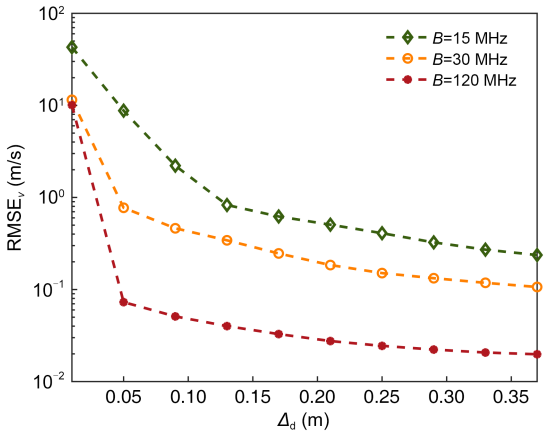

Fig. 8 The RMSE of velocity w.r.t. the range between targets with different signal bandwidths (SNR=15 dB)

greater than 0.045 m and 0.225 m for the 120 MHz and 30 MHz cases, respectively, the estimation accuracy of the proposed CP-NFL algorithm reaches the millimeter level, in which case we can differentiate the two targets. This trend is consistent with the well-known radar theory, which states that as the bandwidth increases, the radar resolution increases. Specifically, by the radar equation, the range resolution is proportional to the bandwidth. Therefore, the range estimation accuracy gradually increases with increasing bandwidth, resulting in a more accurate estimation of the location of the two targets. Moreover, the velocity estimation in Eq. (47) makes use of the estimated location information, so the accuracy of the velocity estimation also increases, which leads to improved velocity resolution.

Fig. 9 illustrates the achievable estimation accuracy with respect to the number of sub-array groups at

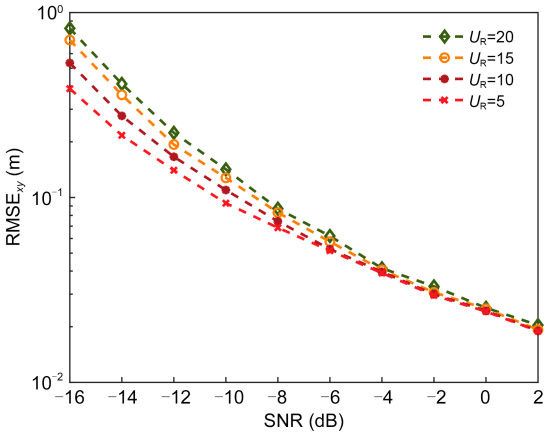

Fig. 9 RMSE of localization w.r.t. the SNR with different numbers of sub-array groups

the receiver. The number of transmit antennas is set to M_T=3, which is considered as one group (U_T=1). The number of receive antennas is set to Q_R=60. Fig. 9 shows that as the number of sub-arrays increases, the estimation accuracy deteriorates. However, this deterioration disappears when the SNR is greater than −4 dB, which is generally the operating case of a system. On the other hand, as analyzed in Section 3.3, dividing the receive antennas into more groups reduces the computational complexity of the proposed algorithm. Therefore, it is necessary to make a reasonable choice between algorithm complexity and estimation accuracy. Fig. 9 further shows that with increasing SNR, the number of groups has less influence on the estimation performance, and when the SNR is high, it is preferable to divide the antennas into a larger number of groups.

Fig. 10 illustrates the effect of velocity on the algorithm. Specifically, the target velocities in the x- and y-direction are identical, that is, $v_x=v_y=v/\sqrt{2}$. This describes the achievable estimation accuracy with respect to the SNR under different velocities v, with the receiving antennas divided into six groups. The localization accuracy gradually deteriorates with increasing velocity. According to Assumption 3 in Section 2, the velocity of the targets relative to the same sub-array antenna is roughly equal. As the velocity increases, Assumption 3 gradually loses validity, and the discrepancy between our signal model and the actual signal model grows, which leads to a deterioration in localization performance.

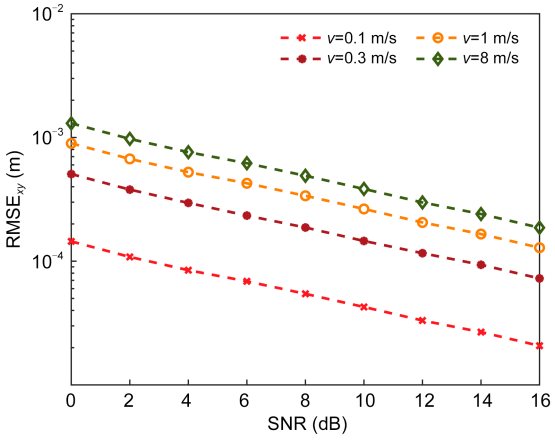

Fig. 10 RMSE of localization w.r.t. the SNR for different velocity cases

5 Conclusions

We propose a CP decomposition-based method for the joint estimation of position and velocity of multiple targets using a terahertz MIMO-OFDM system operating in the near-field region, where the waveforms transmitted from each antenna carry communication messages and are orthogonal to each in the frequency domain. The CP-NFL method exploits the intrinsic multi-dimensional structure of the multi-channel received signal. Specifically, the received signal is expressed as a third-order tensor. We show that the tensor has a low-rank CP decomposition form and use the tensor's decomposed factor matrices to transform the original non-convex optimization problem into a convex one. The investigation of CP decomposition uniqueness revealed that it can be guaranteed, even with a small number of targets. To further reduce the computational complexity of the proposed algorithm, we divide the antennas into several sub-arrays. Our analysis shows that the computational complexity of the proposed method is linear to the sum of the third powers of the number of sub-carriers, OFDM symbols, antennas, and targets. We compare our proposed method with the existing LS-based parameter estimation method using simulations, and demonstrated the impact of system parameters on estimation accuracy, highlighting the advantage of the proposed CP-NFL method.

Contributors

Lingxiang LI and Ke LIU designed the research. Weixin CHEN and Qiang XU processed the data. Shengfu ZHAO drafted the paper. Zhen WANG helped organize the paper. Lingxiang LI and Zhi CHEN revised and finalized the paper.

Conflict of interest

Zhi CHEN is a guest editor of this special issue, and he was not involved with the peer review process of this paper. All the authors declare that they have no conflict of interest.

Data availability

The data that support the findings of this study are available from the corresponding author upon reasonable request.

References

Akyildiz IF, Kak A, Nie S, 2020. 6G and beyond: the future of wireless communications systems. *IEEE Access*, 8:133995-134030. https://doi.org/10.1109/ACCESS.2020.3010896

Akyildiz IF, Han C, Hu ZF, et al., 2022. Terahertz band communication: an old problem revisited and research

directions for the next decade. *IEEE Trans Commun*, 70(6):4250-4285. https://doi.org/10.1109/TCOMM.2022.3171800

Alhafid AK, Younis S, Ali YEM, 2024. Enhanced far-field localization scheme using multi-RIS and efficient beam sweeping. *Prog Electromagn Res C*, 140:163-175. https://doi.org/10.2528/PIERC23112903

Chen H, Sarieddeen H, Ballal T, et al., 2022. A tutorial on terahertz-band localization for 6G communication systems. *IEEE Commun Surv Tutor*, 24(3):1780-1815. https://doi.org/10.1109/COMST.2022.3178209

Chen HY, Ahmad F, Vorobyov S, et al., 2021. Tensor decompositions in wireless communications and MIMO radar. *IEEE J Sel Top Signal Process*, 15(3):438-453. https://doi.org/10.1109/JSTSP.2021.3061937

Cohen D, Cohen D, Eldar YC, et al., 2018. SUMMeR: sub-Nyquist MIMO radar. *IEEE Trans Signal Process*, 66(16): 4315-4330. https://doi.org/10.1109/TSP.2018.2838541

Cui MY, Wu ZD, Lu Y, et al., 2023. Near-field MIMO communications for 6G: fundamentals, challenges, potentials, and future directions. *IEEE Commun Mag*, 61(1):40-46. https://doi.org/10.1109/MCOM.004.2200136

Da Rosa Zanatta M, De Mendonça FLL, Antreich F, et al., 2019. Tensor-based time-delay estimation for second and third generation global positioning system. *Dig Signal Process*, 92:1-19. https://doi.org/10.1016/j.dsp.2019.04.003

De Lathauwer L, 2006. A link between the canonical decomposition in multilinear algebra and simultaneous matrix diagonalization. *SIAM J Matrix Anal Appl*, 28(3):642-666. https://doi.org/10.1137/040608830

Gao JB, Chen XM, Li GY, 2024. Deep unfolding based channel estimation for wideband terahertz near-field massive mimo systems. *Front of Inform Technol Electron Eng*, 25(8): 1162-1172. https://doi.org/10.1631/FITEE.2300760

Gaudio L, Kobayashi M, Bissinger B, et al., 2019. Performance analysis of joint radar and communication using OFDM and OTFS. IEEE Int Conf on Communications Workshops, p.1-6. https://doi.org/10.1109/ICCW.2019.8757044

Knill C, Roos F, Schweizer B, et al., 2019. Random multiplexing for an MIMO-OFDM radar with compressed sensing-based reconstruction. *IEEE Microw Wirel Compon Lett*, 29(4):300-302. https://doi.org/10.1109/LMWC.2019.2901405

Li X, Chang B, Chen Z, 2023. Tensor decomposition based THz channel estimation in OTFS for integrated sensing and communications. IEEE Global Communications Conf, p.3996-4001. https://doi.org/10.1109/GLOBECOM54140.2023.10437761

Liu YJ, Liao GS, Yang ZW, et al., 2017. Design of integrated radar and communication system based on MIMO-OFDM waveform. *J Syst Eng Electron*, 28(4):669-680. https://doi.org/10.21629/JSEE.2017.04.06

Pan YJ, De Bast S, Pollin S, 2021. Indoor direct positioning with imperfect massive MIMO array using measured near-field channels. *IEEE Trans Instrum Meas*, 70:1-11. https://doi.org/10.1109/TIM.2021.3067963

Podkurkov I, Hamidullina L, Traikov E, et al., 2018. Tensor-based near-field localization in bistatic MIMO radar systems. 22nd Int ITG Workshop on Smart Antennas, p.1-8.

Podkurkov I, Seidl G, Khamidullina L, et al., 2021. Tensor-based near-field localization using massive antenna arrays. *IEEE Trans Signal Process*, 69:5830-5845. https://doi.org/10.1109/TSP.2021.3105797

Rinchi O, Elzanaty A, Alouini MS, 2022. Compressive near-field localization for multipath RIS-aided environments. *IEEE Commun Lett*, 26(6):1268-1272. https://doi.org/10.1109/LCOMM.2022.3151036

Sakhnini A, De Bast S, Guenach M, et al., 2022. Near-field coherent radar sensing using a massive MIMO communication testbed. *IEEE Trans Wirel Commun*, 21(8):6256-6270. https://doi.org/10.1109/TWC.2022.3148035

Sanson JB, Castanheira D, Gameiro A, et al., 2019. High-resolution DOA estimation of closely-spaced and correlated targets for MIMO OFDM radar-communication system. IEEE Int Symp on Phased Array System & Technology, p.1-5. https://doi.org/10.1109/PAST43306.2019.9021057

Sarieddeen H, Alouini MS, Al-Naffouri TY, 2021. An overview of signal processing techniques for terahertz communications. *Proc IEEE*, 109(10):1628-1665. https://doi.org/10.1109/JPROC.2021.3100811

Singh PR, Wang Y, Chargé P, 2016. Bistatic MIMO radar for near field source localisation using PARAFAC. *Electron Lett*, 52(12):1060-1061. https://doi.org/10.1049/el.2015.4380

Singh PR, Wang YD, Chargé P, 2017. Near field targets localization using bistatic MIMO system with spherical wavefront based model. 25th European Signal Processing Conf, p.2408-2412. https://doi.org/10.23919/EUSIPCO.2017.8081642

Temiz M, Alsusa E, Baidas MW, 2021. Optimized precoders for massive MIMO OFDM dual radar-communication systems. *IEEE Trans Commun*, 69(7):4781-4794. https://doi.org/10.1109/TCOMM.2021.3068485

Tian TW, Zhang TX, Kong LJ, et al., 2021. Transmit/receive beamforming for MIMO-OFDM based dual-function radar and communication. *IEEE Trans Veh Technol*, 70(5):4693-4708. https://doi.org/10.1109/TVT.2021.3072094

Tsujimura K, Mori H, 2022. Near field DoA estimation utilizing a large aperture MIMO array radar with Tx beamforming. 18th European Radar Conf, p.137-140. https://doi.org/10.23919/EuRAD50154.2022.9784552

Wan T, Liu Q, Du XF, et al., 2023. Performance analysis of joint range and velocity estimator for e-band ISAC. IEEE Wireless Communications and Networking Conf, p.1-5. https://doi.org/10.1109/WCNC55385.2023.10118736

Xiao M, Mumtaz S, Huang YM, et al., 2017. Millimeter wave communications for future mobile networks. *IEEE J Sel Areas Commun*, 35(9):1909-1935. https://doi.org/10.1109/JSAC.2017.2719924

Zhang HY, Shlezinger N, Guidi F, et al., 2022. Near-field wireless power transfer for 6G Internet of Everything mobile

networks: opportunities and challenges. *IEEE Commun Mag*, 60(3):12-18. https://doi.org/10.1109/MCOM.001.2100702

Zhang HY, Shlezinger N, Guidi F, et al., 2023. 6G wireless communications: from far-field beam steering to near-field beam focusing. *IEEE Commun Mag*, 61(4):72-77. https://doi.org/10.1109/MCOM.001.2200259

Zhang JA, Liu F, Masouros C, et al., 2021. An overview of signal processing techniques for joint communication and radar sensing. *IEEE J Sel Top Signal Process*, 15(6):1295-1315. https://doi.org/10.1109/JSTSP.2021.3113120

Zhang RY, Cheng L, Wang S, et al., 2023. Target sensing in wideband massive MIMO-ISAC systems in the presence of beam squint. IEEE Int Conf on Communications Workshops, p.931-936. https://doi.org/10.1109/ICCWorkshops57953.2023.10283625

Zhang XF, Chen WY, Zheng W, et al., 2018. Localization of near-field sources: a reduced-dimension music algorithm. *IEEE Commun Lett*, 22(7):1422-1425. https://doi.org/10.1109/LCOMM.2018.2837049

Zhao BB, Hu KK, Wen FX, et al., 2023. TDLoc: passive localization for MIMO-OFDM system via tensor decomposition. *IEEE Int Things J*, 10(23):20819-20833. https://doi.org/10.1109/JIOT.2023.3283991

Zuo WL, Xin JM, Liu WY, et al., 2019. Localization of near-field sources based on linear prediction and oblique projection operator. *IEEE Trans Signal Process*, 67(2):415-430. https://doi.org/10.1109/TSP.2018.2883034

Appendix: proof of Lemma 2

According to Eq. (33), x_l and $\rho^{\mathrm{R}}_{M_{\mathrm{R}}/2,l}$ can be directly obtained by the LS algorithm, which is

$$\begin{bmatrix} \bar{x}_l \\ \bar{\rho}^{\mathrm{R}}_{M_{\mathrm{R}}/2,l} \end{bmatrix}=\left(\boldsymbol{P}^{\mathrm{T}}\boldsymbol{P}\right)^{-1}\boldsymbol{P}^{\mathrm{T}}\boldsymbol{h}_l. \tag{A1}$$

However, Podkurkov et al. (2018) indicated that the accuracy of range $\hat{\rho}^{\mathrm{R}}_{Q_{\mathrm{R}}/2,l}$ estimation decreases seriously as the distance to the target increases, which would cause deterioration of the localization performance. Fortunately, the estimation of θ_l (the azimuth of the target relative to the $(Q_{\mathrm{R}}/2)^{\mathrm{th}}$ receiving antenna, Fig. 2) is highly accurate (Podkurkov et al., 2018). Thus, we use $\hat{x}_l$ and $\hat{\rho}^{\mathrm{R}}_{Q_{\mathrm{R}}/2,l}$ to estimate θ_l. According to the geometric relationship between the target and the center of the receive antenna array, we have

$$x_l=\rho^{\mathrm{R}}_{Q_{\mathrm{R}}/2,l}\cos\theta_l+x_{\mathrm{R},Q_{\mathrm{R}}/2}, \tag{A2}$$

which, combined with $\hat{x}_l$, $\hat{\rho}^{\mathrm{R}}_{M_{\mathrm{R}}/2,l}$, indicates that

$$\hat{\theta}_l=\arccos\left(\frac{\bar{x}_l-x_{\mathrm{R},Q_{\mathrm{R}}/2}}{\bar{\rho}^{\mathrm{R}}_{Q_{\mathrm{R}}/2,l}}\right). \tag{A3}$$

To determine the rough position of the target, the azimuth information and distance information are needed. The azimuth information $\hat{\theta}_l$ is estimated and the distance information is contained in $\hat{\tau}_{M_{\mathrm{T}}/2,Q_{\mathrm{R}}/2,l}$. Thus, in the following, we use the estimated $\hat{\theta}_l$ and delay $\hat{\tau}_{M_{\mathrm{T}}/2,Q_{\mathrm{R}}/2,l}$ to jointly derive x_l and $\rho^{\mathrm{R}}_{Q_{\mathrm{R}}/2,l}$.

Substituting the estimated parameters $\hat{\theta}_l$ and $\hat{\tau}_{M_{\mathrm{T}}/2,Q_{\mathrm{R}}/2,l}$ into Eqs. (A2) and (36), respectively, we have

$$\begin{aligned} x_l&=\rho^{\mathrm{R}}_{Q_{\mathrm{R}}/2,l}\cos\hat{\theta}_l+x_{\mathrm{R},Q_{\mathrm{R}}/2},\\ \rho^{\mathrm{R}}_{Q_{\mathrm{R}}/2,l}&=c\hat{\tau}_{M_{\mathrm{T}}/2,Q_{\mathrm{R}}/2,l}-\sqrt{(\rho^{\mathrm{R}}_{Q_{\mathrm{R}}/2,l})^2+2x_l\xi}\,. \end{aligned} \tag{A4}$$

Solving Eq. (A4), we arrive at

$$\begin{aligned} \breve{\rho}^{\mathrm{R}}_{Q_{\mathrm{R}}/2,l}&=\frac{\left(c\hat{\tau}_{M_{\mathrm{T}}/2,Q_{\mathrm{R}}/2,l}\right)^2+2\xi^2}{2c\hat{\tau}_{M_{\mathrm{T}}/2,Q_{\mathrm{R}}/2,l}-2\cos\hat{\theta}_l\xi},\\ \breve{x}_l&=\breve{\rho}^{\mathrm{R}}_{Q_{\mathrm{R}}/2,l}\cos\hat{\theta}_l+x_{\mathrm{R},Q_{\mathrm{R}}/2}. \end{aligned} \tag{A5}$$

This completes the proof.